Restacking-Inhibited 3D Reduced Graphene Oxide for High Performance Supercapacitor Electrodes

Ji Hoon Lee,[†] Nokyoung Park,[‡] Byung Gon Kim,[†] Dae Soo Jung,[†] Kyuhyun Im,[‡] Jaehyun Hur,[‡,*] and Jang Wook Choi[†,§,*]

[†]Graduate School of EEWS (WCU), Korea Advanced Institute of Science and Technology (KAIST), 291 Daehak-ro, Yuseong Gu, Daejeon 305-701, Republic of Korea, [‡]Frontier Research Laboratory, Samsung Advanced Institute of Technology, Samsung Electronics, Yongin, Kyunggi-do 446-712, Republic of Korea, and [§]KAIST Institute Nano Century, Korea Advanced Institute of Science and Technology (KAIST), 291 Daehak-ro, Yuseong Gu, Daejeon, 305-701, Republic of Korea.

The manuscript was written through contributions of all authors. All authors have given approval to the final version of the manuscript

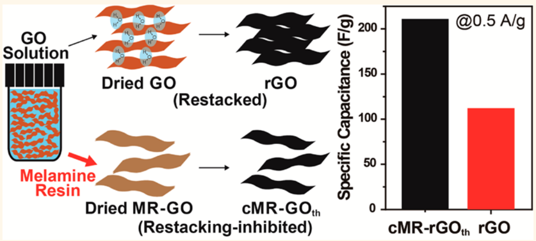

ABSTRACT Graphene has received considerable attention in both scientific and technological areas due to its extraordinary material properties originating from the atomically single- or small number-layered structure. Nevertheless, in most scalable solution-based syntheses, graphene suffers from severe restacking between individual sheets and thus loses its material identity and advantages. In the present study, we have noticed the intercalated water molecules in the dried graphene oxide (GO) as a critical mediator to such restacking and thus eliminated the hydrogen bonding involving the intercalated water by treating GO with melamine resin (MR) monomers. Upon addition of MR monomers, porous restacking-inhibited GO sheets precipitated, leading to the carbonaceous composite with an exceptionally large surface area of 1040 m^2/g after a thermal treatment. Utilizing such high surface area, the final graphene composite exhibited excellent electrochemical performance as a supercapacitor electrode material: specific capacitance of 210 F/g, almost no capacitance loss for 20 000 cycles, and ~7 s rate capability. The current study delivers a message that various condensation reactions engaging GO sheets can be a general synthetic approach for restacking-inhibited graphene in scalable solution processes.

KEYWORDS: condensation reaction · melamine resin · reduced graphene oxide · restacking · supercapacitor · nitrogen doping

As energy and environmental issues caused by the use of fossil fuels have become serious, utilization of renewable energy resources represented by solar and wind energy has been increasingly critical. For efficient use of these renewable energy resources, grid-scale energy storage systems (ESSs) are essential because availability of those resources fluctuates with time.[1,2] Along this direction, supercapacitors (SCs) have attracted a great deal of attention as one of ESSs because their innate high power capabilities (~10 kW/kg) can support momentary loading and energy smoothing, which are crucial in operations of grid-type ESSs.[3−8] Long lifetimes (>100 000 cycles) of SCs are also desirable for operations of such ESSs. In addition, SCs have been often considered in combined systems with rechargeable batteries for ESSs because the short-term transient issues inevitable during electric grid operations are beyond rate capabilities of typical rechargeable batteries. Besides ESSs, SCs are expanding their territories into various applications where high power operations are required, and cordless electric tools and hybrid electrical vehicles (HEVs) are representative examples.[9−11]

In one class of SCs, so-called electrical double layer capacitors (EDLCs), the energy is stored and released by adsorption and desorption of carrier ions in the EDLs on the electrode surface.[10,12−25] Thus, the capacitance is by and large proportional to the surface area of the electrode, which renders various carbonaceous nanomaterials attractive as SC electrodes. For this reason, the carbon community has intensively investigated activated carbons (ACs),[20,21] carbon nanotubes (CNTs),[22−24,26] carbon nanofibers (CNFs),[25] and graphene[3,12−16,19,27,28] for SC electrodes. Among this wide range of carbon nanomaterials, graphene, 2-dimensional (2D) hexagonal lattice of sp^2 hybridized carbon atoms, has been counted as a

* Address correspondence to:
jaehyun.hur@samsung.com,
jangwookchoi@kaist.ac.kr.

Received for review August 5, 2013
and accepted September 3, 2013.

10.1021/nn4040734

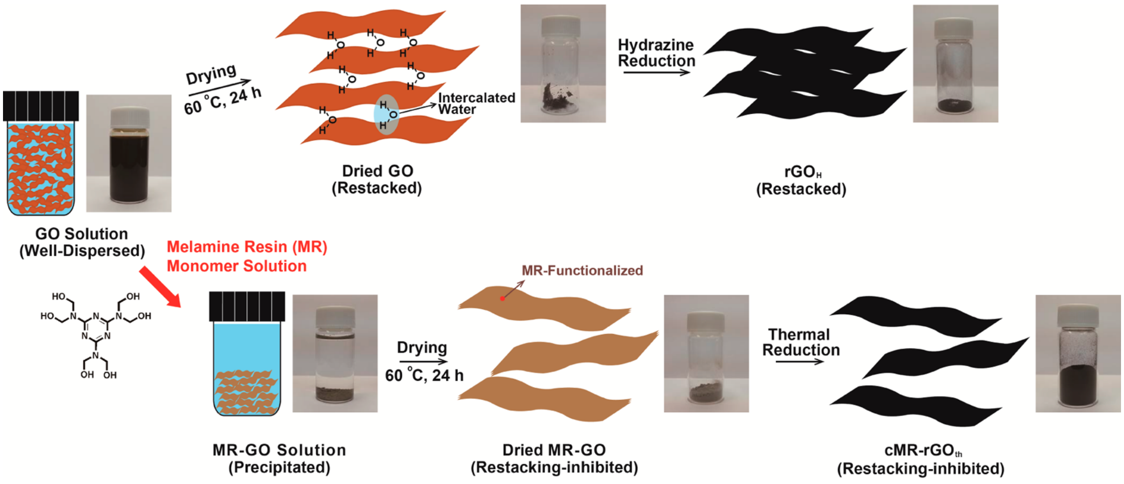

Figure 1. Schematic illustrations showing the synthetic routes of rGO$_H$ and cMR-rGO$_{th}$. The addition of melamine resin monomer solution is a key step for the restacking inhibition of the final cMR-rGO$_{th}$.

promising candidate because of its high electrical conductivity and exceptionally large theoretical specific surface area (~2650 m^2/g).[14,18] For reference, it was reported that such a high theoretical surface area can afford to deliver a gravimetric capacitance of SC as high as 550 F/g.[29] Despite this promising intrinsic property, when prepared in the form of reduced graphene oxide (rGO) *via* established solution processes, namely *via* Hummer's method, typical graphene SCs exhibit only 100−120 F/g in organic electrolytes.[13,15,19,30,31] These smaller specific capacitances originate mainly from irreversible restacking of the individual rGO sheets during the reduction and drying processes,[15,32,33] which make substantial surfaces of rGO unavailable for charge storage. The vulnerable restacking during the established synthetic procedure implies that the capacitances of graphene SCs are largely dependent on the detailed characteristics of graphene such as its functional groups, size, pore structure, and surface accessibility.[3,10,18,19]

In order to address the restacking issue of graphene sheets, it is necessary to clarify the origin of the phenomenon. It has been known that, in Hummer's method, one or a small number of GO sheets are highly dispersed in the GO solution.[16,32−37] Interestingly, even after the GO solution is dried, water molecules remain stuck in the GO powder *via* hydrogen bonding interactions[16,33−36] between water molecules and oxygen-containing functional groups of GO (Figure 1), and these water molecules are often referred to as "intercalated" water molecules. The intercalated water molecules play a decisive role in the restacking of the final rGO because the hydrogen bonding facilitates interactions between GO sheets, resulting in aligning the GO sheets in the same orientations.[16,33,34] Having noticed the critical role of the intercalated water molecules for the restacking of graphene, in the present study, we functionalized GO sheets with melamine resin (MR) monomers[38−40] to prevent the hydrogen bonding with water molecules upon drying. Consequently, after carbonization of MR monomers, the final graphene powder holds substantially reduced restacking as well as resultant macro-/mesopores and, as a consequence, delivers significantly improved electrochemical performance when tested as supercapacitor electrodes.

RESULT AND DISCUSSION

Figure 1 comparatively illustrates the synthetic routes of the restacking-inhibited rGO, the structure of interest in the current investigation, and the conventional rGO. Both synthetic routes start from the GO solution, but, at this initial stage, the restacking-inhibited case involves a MR treatment, resulting in dramatic differences in the microscopic morphologies. As described above, in the case of rGO, the dried GO contains intercalated water molecules through the hydrogen bonding that facilitates the restacking to a large degree even at this intermediate stage.[16,33−35] Upon subsequent reduction by a hydrazine treatment, the restacking is transferred to the final rGO *via* van der Waals forces between rGO sheets.[15,32] By contrast, the MR-functionalized GO (denoted as MR-GO) eliminates the hydrogen bonding by a condensation reaction[38−42] of the hydroxyl end groups of MR monomers with the hydroxyl or carboxylic acid groups on the GO sheets: $R^1\text{-OH (MR)} + R^2\text{-OH (GO)} \rightarrow R^1\text{-O-}R^2 \text{ (MR-GO)} + H_2O$. Therefore, the restacking is inhibited at the dried MR-GO stage, and such a restacking-inhibited characteristic is preserved through the end of the subsequent carbonization. In the actual experiment, after a certain point when the GO solution was continuously added to the MR monomer solution, bright brown colored MR-GO started to precipitate spontaneously because of increased hydrophobicity of the GO sheets as the condensation reactions proceeded.

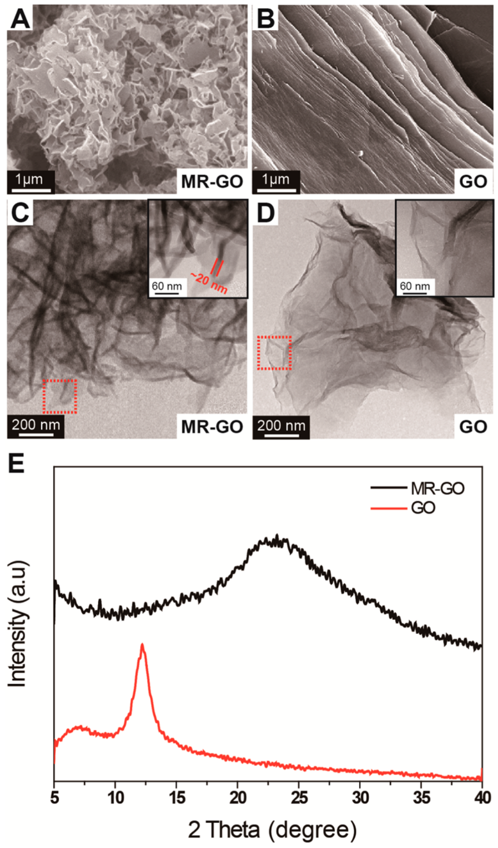

Figure 2. SEM images of (A) MR-GO and (B) GO. (C and D) TEM images and (E) XRD spectra for the same samples.

TABLE 1. Element Contents of GO, MR-GO, rGO_H, and $cMR\text{-}rGO_{th}$ Obtained by XPS Analysis

	C (atomic %)	N (atomic %)	O (atomic %)
GO	66.60	0	33.40
MR-GO	56.20	35.00	8.80
rGO_H	82.00	2.31	15.69
$cMR\text{-}rGO_{th}$	86.76	5.24	8.00

The restacking-inhibited nature of MR-GO was reflected in scanning electron microscopy (SEM) and transmission electron microscopy (TEM) characterizations. When both samples were compared on the micrometer scale, a crumpled morphology in the range of tens to hundreds of nanometers was observed (Figure 2A), which may be the first indication of the restacking-inhibited nature of MR-GO. By contrast, the dried GO appeared as micrometer-scale particles with densely stacked structures (Figure 2B). Such distinctive morphologies between both samples were characterized more closely by TEM characterization. MR-GO showed the individual sheets scattered in random 3D orientations (Figure 2C), whereas the GO sheets in the dried GO appeared by and large aligned along the TEM grid (Figure 2D). More comprehensive SEM images of MR-GO in different magnifications are presented in Figure S1 (Supporting Information). In the high magnification TEM images of MR-GO (Figure 2C, inset), dark lines corresponding to the cross sections of the individual MR-GO flakes were frequently observed. From the average thickness of these dark lines (~20 nm), it turns out that each graphene flake constituting local structure of the MR-GO powder consists of approximately several sheets of MR-functionalized GO considering the thickness (0.6–1.2 nm) of each GO sheet[35,43,44] and the presence of MR on the GO surfaces. In the case of the dried GO (Figure 2D, inset), the black/white contrasts were much less pronounced because of its restacked characteristic.

X-ray diffraction (XRD) analyses also provide structural information on both samples (Figure 2E), particularly focusing on the crystallinity and interlayer distance. The dried GO powder exhibited a sharp peak at $2\theta = 12.3°$,[35,43,44] which is indicative of decent crystallinity of aligned GO layers along their stacks and increased interlayer distance (~7.25 Å) due to the oxygen-containing functional groups and the intercalated water molecules. On the contrary, the MR-GO powder showed only a broad peak at $2\theta = 24°$,[19,43,44] which corresponds to the moderately aligned graphitic arrays along the (002) direction. These graphitic arrays indeed correspond to the graphene flakes appearing as the dark lines in the TEM image in Figure 2C. The elemental analyses using X-ray photoelectron spectroscopy (XPS) also suggest a consistent picture (Table 1 and Figure S2A, Supporting Information). The eliminated hydrogen bonding in MR-GO was reflected in its substantially smaller oxygen content (8.80%) compared to that (33.40%) of the dried GO powder.[41,42]

Moreover, the restacking-inhibited character of MR-GO was transferred to the same sample even after thermal reduction. During this thermal treatment, MR was carbonized simultaneously, so we denote this thermal-treated sample as $cMR\text{-}rGO_{th}$. As in the case of MR-GO, $cMR\text{-}rGO_{th}$ exhibited a wrinkled morphology in the range of tens to hundreds of nanometers under SEM characterization (Figures 3A and S3, Supporting Information) as well as its scattered individual or small number of rGO sheets in the sub-20 nm scale under TEM characterization (Figure 3B). The observed morphologies containing void space in various dimensions are indeed reflected in a wide range of pore sizes in the porosity measurements, which will be described in the next paragraph. The restacking-inhibited morphologies of both MR-GO and $cMR\text{-}rGO_{th}$ were also visualized in scanning transmission electron microscopy (STEM) images (Figure S4, Supporting Information). In addition, the XPS elemental analyses of both samples indicate that the carbon content increased from 56.20% (MR-GO) to 86.76% ($cMR\text{-}rGO_{th}$) (Table 1 and Figure S2A,B, Supporting Information), suggesting that most of MR was carbonized after the thermal treatment. Indeed, the carbon content of

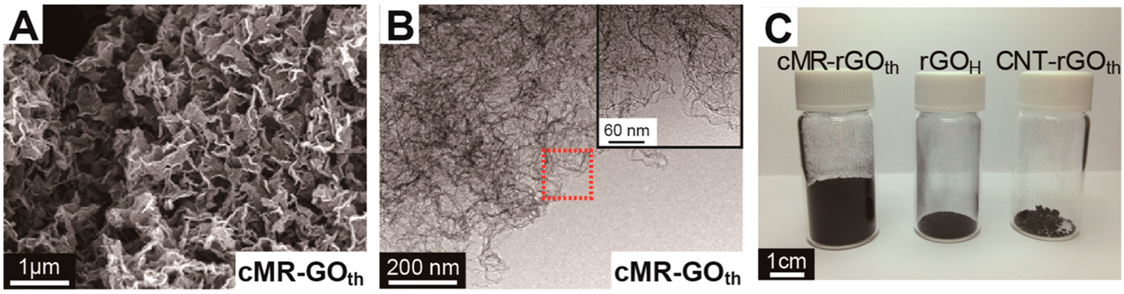

Figure 3. (A) SEM and (B) TEM image of cMR-rGO$_{th}$. (C) Photograph of cMR-rGO$_{th}$, rGO$_H$, and CNT-rGO$_{th}$ with the same masses (70 mg) in 10 mL vials.

cMR-rGO$_{th}$ is comparable to that (82.00%) of the well-established rGO reduced by hydrazine (denoted as rGO$_H$). On the other hand, the high resolution N 1s XPS data exhibited two peaks at 398.4 and 400.9 eV corresponding to the N-6 (pyridine-like) and N-Q (graphite-like) nitrogen configurations, respectively (Figure S2C, Supporting Information). These N-configurations are consistent with previous reports[38−42] on similar MR-originating materials and are also expected to enhance the electrical conductivity of cMR-rGO$_{th}$ *via* excess electrons of N-Q.[13,19,20,39]

Even before quantitative porosity measurements, the volume of the sample at the given mass indicates drastic difference in the porosity between the samples. For a more thorough comparison, we added CNT-rGO$_{th}$ composite as another control sample (see its SEM image in Figure S5, Supporting Information). The synthetic procedure of this control sample is described in the Experimental Section. For the same mass of 70 mg, cMR-rGO$_{th}$ exhibited a markedly larger volume compared to those of the other two controls (Figure 3C), reflecting the restacking-inhibited characteristic of cMR-rGO$_{th}$. N_2 adsorption/desorption analyses gave more quantitative set of information on the porosities of cMR-rGO$_{th}$ and rGO$_H$ (Figure 4A−D). cMR-rGO$_{th}$ exhibited a type IV isotherm with a small hysteresis around $P/P_0 = 0.9$ (Figure 4A), indicating coexistence of macropores and mesopores in the given powder, which is consistent with the SEM image in Figure 3A. By contrast, rGO$_H$ exhibited a different isotherm shape with a large hysteresis in the P/P_0 range of 0.5−1.0 (Figure 4B), indicating the dominant presence of relatively small mesopores existing between the restacked rGO$_H$ sheets.[32,33,45] From these isotherms, it turned out that cMR-rGO$_{th}$ holds remarkably higher surface area and pore volume than those of rGO$_H$ when analyzed on the basis of the Brunauer−Emmett−Teller (BET) and Barrett−Joyner−Halenda (BJH) model, respectively: 1040 *versus* 466 m^2/g and 2.6 *versus* 0.6 cm^3/g.

The pore size distributions (PSDs) obtained on the basis of the density functional theory (DFT) method in the adsorption branches also deliver a consistent picture in the pore size viewpoint. cMR-rGO$_{th}$ exhibited a large portion of pores in the range of 50−80 nm (Figure 4C), which originate from the pore formation between the rGO flakes. By contrast, most of the pores in rGO$_H$ turned out to be in the sub-10 nm region (Figure 4D), which is again associated with the small meso- and micropores formed between the rGO sheets during their irreversible restacking.[32] The PSDs attained from the BJH method (Figure S6, Supporting Information) also showed consistent results regarding the prevailing pore dimensions of both samples. The given pore dimension of cMR-rGO$_{th}$ would be more suitable for diffusion of carrier ions compared to those of conventional activated carbons comprised mainly of micropores and small mesopores. It has been found[21] that these pore dimensions of most activated carbons are too small for ionic diffusion, thus leading to the situation that a good portion of the surface area does not participate in the actual charge storage. The N_2 adsorption−desorption isotherms of CNT-rGO$_{th}$ and CNTs are presented in Figure S7 (Supporting Information), and the porosity data of all the samples are summarized in Table 2. The XRD spectra (Figure 4E) of cMR-rGO$_{th}$ and rGO$_H$ also provide distinctive structural characteristics of both samples. Although both spectra showed the peaks at $2\theta = 24°$ corresponding to the (002) plane of the graphitic array,[19,43,44] the peak of cMR-rGO$_{th}$ was broader than that of rGO$_H$ because of the restacking-inhibited characteristic of cMR-rGO$_{th}$.

In order to assess the restacking-inhibition effect on the electrochemical performance, we evaluated cMR-rGO$_{th}$ as an active material of symmetric SC electrodes by preparing coin-cells. Most electrochemical characterizations were conducted under galvanostatic mode in the potential range of 0−2.0 V. Detailed cell preparation and measurement conditions are described in the Experimental Section. Other control samples including rGO$_H$, CNT-rGO$_{th}$, and CNTs were also tested for comparison. Figure 5A displays the typical galvanostatic profiles measured at the same current density of 0.5 A/g for cMR-rGO$_{th}$ and rGO$_H$. The significantly longer charging and discharging durations for cMR-rGO$_{th}$ indicates its superior capacitance to that of rGO$_H$. Even when compared against CNT-rGO$_{th}$ and CNTs (Figure 5B), the capacitance of cMR-rGO$_{th}$ turned out to be far higher. At the same current density of 0.5 A/g,

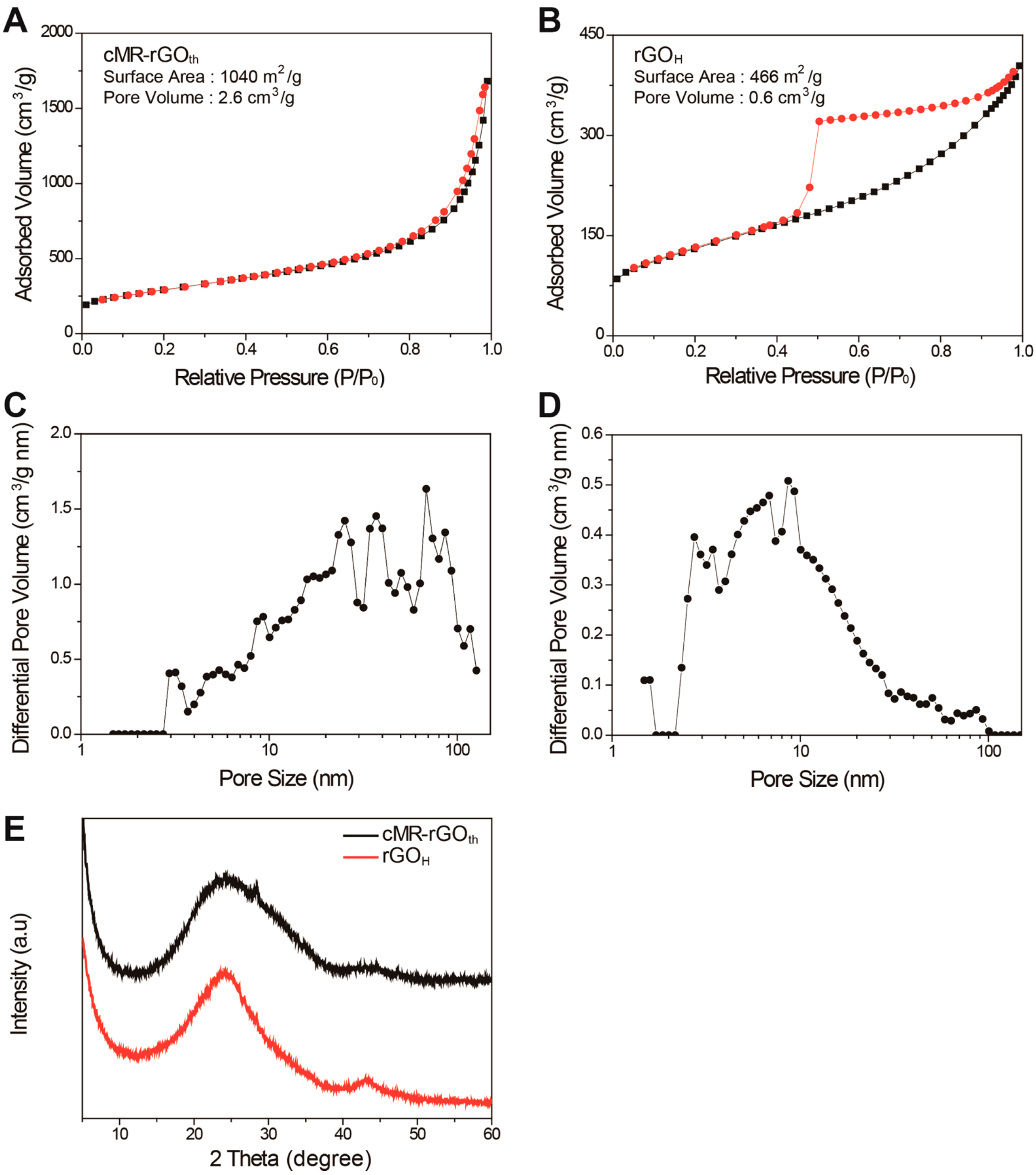

Figure 4. Nitrogen adsorption−desorption isotherms of (A) cMR-rGO$_{th}$ and (B) rGO$_H$. The black and red lines correspond to the adsorption and desorption curves, respectively. The pore size distributions of (C) cMR-rGO$_{th}$ and (D) rGO$_H$. (E) The XRD patterns of cMR-rGO$_{th}$ (black) and rGO$_H$ (red).

TABLE 2. Specific Surface Areas, Pore Volumes, and Specific Capacitances of All the Carbonaceous Materials in This Study

	specific surface area (m^2/g)	pore volume (cm^3/g)	specific capacitance (F/g @0.5 A/g)
cMR-rGO$_{th}$	1040	2.6	210
rGO$_H$	466	0.6	110
CNT-rGO$_{th}$	233	0.9	33
CNTs	176	0.7	15

cMR-rGO$_{th}$, rGO$_H$, CNT-rGO$_H$, and CNTs exhibited 210, 110, 33, and 15 F/g, respectively. The capacitive nature of cMR-rGO$_{th}$ and its superior capacitance compared to that of rGO$_H$ were also confirmed by the cyclic voltammetry results (Figure S8, Supporting Information). From these distinctive capacitances, the following points are noteworthy:

(1) cMR-rGO$_{th}$ showed ∼2 times higher specific capacitance compared to that of rGO$_H$, which is indicative of critical morphology effect on the capacitance as well as significance of restacking-inhibition by the MR-treatment toward increased capacitance. Also, the increased nitrogen content (2.31 *versus* 5.24%) must contribute to the improved capacitance, because N-doped sites[13,39] have been known to hold

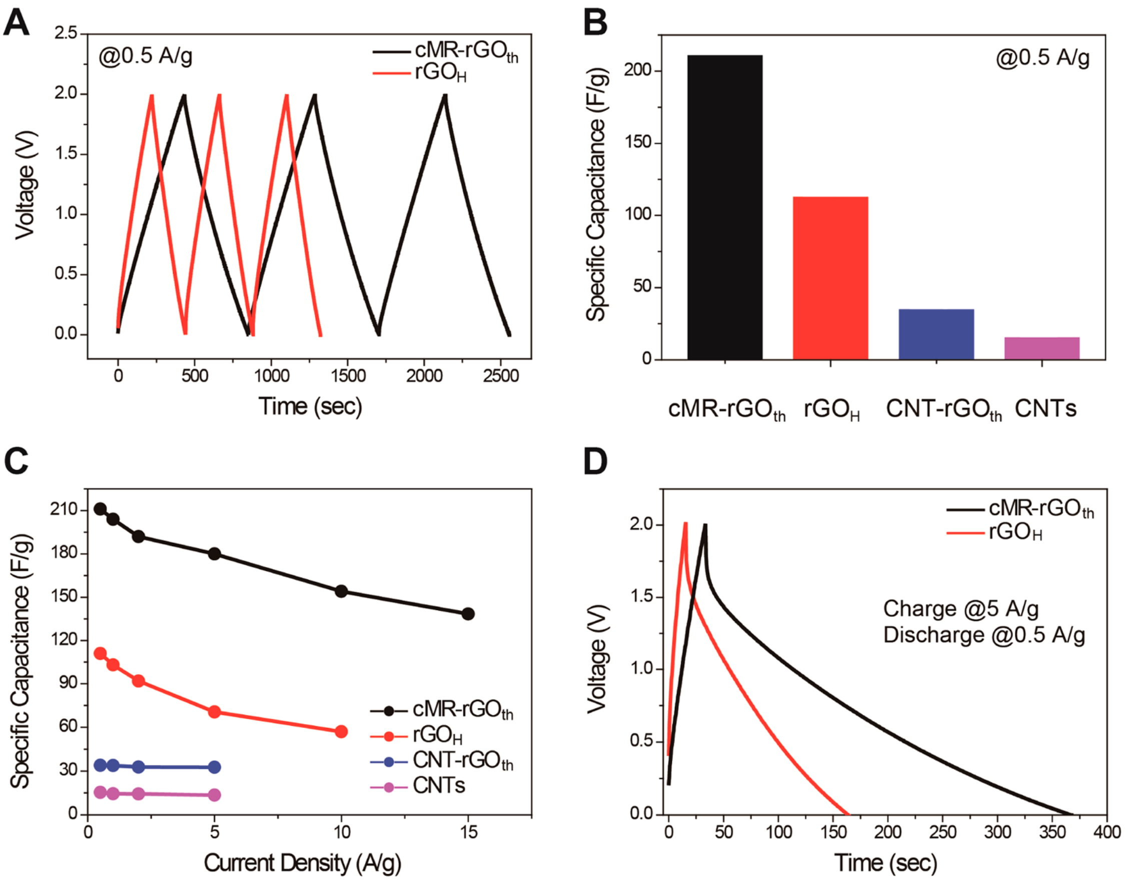

Figure 5. (A) Charge and discharge profiles of cMR-rGO$_{th}$ (black) and rGO$_H$ (red) when measured at the same current density of 0.5 A/g. (B) The specific capacitances of all of the samples investigated in this study when all of them were measured at the same current density of 0.5 A/g. (C) The gravimetric capacitances of all of the four samples at various current densities. (D) Fast charging and slow discharging tests of cMR-rGO$_{th}$ and rGO$_H$ to evaluate the given samples as future flash energy storage devices. 5.0 and 0.5 A/g were applied for the fast charging and slow discharging, respectively.

higher affinities with carrier ions particularly through the pyridine-like (N-6) nitrogen sites.

(2) Even though CNTs are largely free from severe restacking, CNTs exhibited the lowest capacitance, which is ascribed to the large inner tube surfaces that do not contribute substantially to adsorption of carrier ions as well as the absence of edge sites that has been known to have higher affinity to carrier ions than basal planes.[46−49] Although the capacitance of CNTs appears to be too small, the value is indeed consistent with the reported.[23] This capacitance may be improved to some degree by replacing multiwall CNTs with single-wall CNTs.[22,26]

(3) It turned out that CNTs are less effective than MR in alleviating the restacking of rGO in the final composite. This difference must be related to how efficient the given treatment prevents the hydrogen bonding between the intercalated water and GO sheets and thus the restacking at the dried GO stage (Figure 1). In this sense, it can be concluded that the well-defined condensation reactions between MR monomers and the significant portion of GO functional groups are very effective in mitigating the hydrogen bonding and consequently restacking of the final rGO.

Furthermore, the superior capacitance of cMR-rGO$_{th}$ was preserved at higher current densities (Figure 5C). Even at the 20-fold increased current density (10 A/g), 154 F/g was maintained, corresponding to 73% capacitance retention with respect to the capacitance at the original current density. At the same increase in the current density, rGO$_H$ exhibited only 51% capacitance retention (111 → 57 F/g), implying that the well-developed pore structure of cMR-rGO$_{th}$ originating from the restacking-inhibition plays a role for efficient ion diffusion especially at high current densities. The substantial content of the N-Q configuration must also assist the superior rate performance by enhanced electronic conductivity.[13,39] Utilizing these combined effects, cMR-rGO$_{th}$ delivered a high specific capacitance of 140 F/g even at a higher current density of 15 A/g. On the basis of the capacitances of cMR-rGO$_{th}$ obtained at various current densities, we have constructed a Ragone plot (Figure S9, Supporting Information). Consistently, cMR-rGO$_{th}$ showed higher energy densities at the given power densities compared against the other control cases, again taking advantage of the restacking-inhibited structure of cMR-rGO$_{th}$.

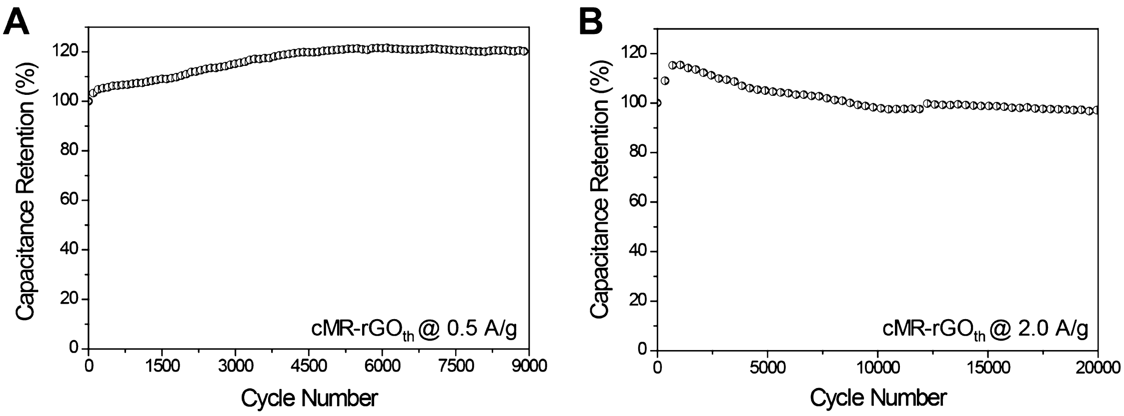

Figure 6. The cycling performance of cMR-rGO$_{th}$ measured at (A) 0.5 A/g and (B) 2.0 A/g.

Additional SC measurements were carried out to reflect the actual operations of portable electronics and EVs where quick charging and slow discharging properties are on higher demand. We therefore tested cMR-rGO$_{th}$ and rGO$_{H}$ under fast charging at 5 A/g but slow discharging at 0.5 A/g (Figure 5D). Even under such a fast charging mode, cMR-rGO$_{th}$ showed a specific capacitance of ~180 F/g, which is 2.5 times larger than that of rGO$_{H}$ (~70 F/g) measured under the same conditions, suggesting that the excellent SC performance of cMR-rGO$_{th}$ is translated to the more challenging operating conditions with the fast charging. This result implies that cMR-rGO$_{th}$ can be a viable option as an electrode material for upcoming flash charging SC applications. In addition, cMR-rGO$_{th}$ exhibited excellent cycling performance (Figures 6A,B). When measured at 0.5 A/g (Figure 6A), its specific capacitance gradually increased in the first 5000 cycles, reaching 120% of the initial value, which might be associated with certain activation processes such as gradual wetting of the electrolyte deep inside the electrode film but requires further characterization for complete understanding. Similar capacitance increase with cycling was also observed previously in other porous electrodes.[16] The increased capacitance remained saturated until 9000 cycles. Notably, this cycle number corresponds to 3 months of continuous measurement. For long-term cycling tests, we also tested cMR-rGO$_{th}$ at a higher current density of 2 A/g (Figure 6B), and cMR-rGO$_{th}$ persistently exhibited excellent capacitance retention of 96% even after 20 000 cycles. Compared to the capacitance retention at 0.5 A/g, the initial capacitance increase at 2 A/g reached the saturation point in the earlier cycling number perhaps because the lesser degree of the electrode surface is involved in the charge storage due to the reduced charge/discharge times. It is noteworthy that rGO used as a control sample in the current study was reduced by the hydrazine-based solution process instead of other well-known thermal treatments. We chose the solution reduction process for fair comparison with cMR-rGO$_{th}$ because it has been found[19] that the solution-reduced rGO exhibits higher capacitances than those of the thermal-reduced rGO.

CONCLUSION

In conclusion, we have addressed the chronic restacking issue of rGO in the conventional solution process and have thus demonstrated remarkably improved SC performance. In particular, having noticed that the intercalated water molecules at the early dried GO stage play a pivotal role in the restacking of the final rGO, we functionalized GO in the solution state with MR monomers to prevent the hydrogen bonding that would keep the intercalated water within the GO powder. As a result, the final cMR-rGO$_{th}$ is endowed with high surface area (~1040 m^2/g) and pore volume (~2.6 cm^3/g) and consequently exhibited excellent performance as a SC electrode in various electrochemical aspects. Overall, the series of the results obtained from cMR-rGO$_{th}$ suggest that various condensation reactions engaging the GO sheets in the solution state can be a general design principle for synthesis of restacking-inhibited rGO in scalable solution processes.

EXPERIMENTAL SECTION

Preparation of cMR-rGO$_{th}$, rGO$_{H}$, and CNT-rGO$_{th}$. Graphite powder (Alfa Aesar, APC 7−11) was first oxidized by a modified Hummer's method to obtain GO. Two grams of graphite and 1 g of sodium nitrate ($NaNO_3$, Sigma Aldrich) were mixed in sulfuric acid (H_2SO_4, 50 mL, Sigma Aldrich) by rigorous stirring for 3 h in an ice bath at 0 °C. Eight grams of potassium permanganate ($KMnO_4$, Sigma Aldrich) was then added slowly into the suspension, and the suspension was stirred until its color turned dark gray. Next, deionized (DI) water (96 mL) was slowly added to the suspension, and the suspension was maintained at 98 °C for 1 h. Finally, warm DI water (280 mL) and hydrogen peroxide solution (H_2O_2, 50 wt %, 20 mL, Sigma Aldrich) were slowly added to obtain a bright brown graphite oxide solution. This solution was filtered and washed with DI water several times, followed by a drying step to obtain "graphite oxide powder".

The next step was to obtain GO solution from the graphite oxide powder by sonication. Typically, 4.2 g of the graphite oxide powder was added to 350 mL of DI water, and this solution was tip-sonicated at 80 W for 2 h. The sonicated solution was centrifuged for 1 h at 9500 rpm. The supernatant solution was dried, and the GO powder was obtained.

cMR-rGO$_{th}$ was prepared by first functionalizing GO sheets with melamine resin (MR-GO), followed by a heat treatment under a vacuum (0.05 bar). For this, MR solution was first prepared by adding 2.5 g of melamine (Sigma Aldrich) and 4.425 mL of 37 wt % formaldehyde aqueous solution (Sigma Aldrich) into 40 mL of DI water. After this solution was heat-treated at 70 °C for 10 min, the solution turned transparent, indicating good solubility of MR monomer in aqueous media. The GO solution (20 mL, 10 mg/mL) was then introduced to the MR monomer solution and stirred at 98 °C for 3 h. During the stirring, the condensation reaction between MR and GO sheets took place, and bright brown MR-GO powder precipitated. This MR-GO was thoroughly washed with DI water and ethanol several times. Finally, cMR-rGO$_{th}$ was obtained by a multistep heat treatment of MR-GO (120 °C for 20 min, 400 °C for 2 h, 600 °C for 2 h, and 800 °C for 2 h) with a ramping rate of 1 °C/min.

rGO$_H$ was prepared as a control sample by reducing 200 mL of the 1 mg/mL GO solution with 400 μL of hydrazine monohydrate ($H_2N-NH_2 \cdot H_2O$, Sigma Aldrich).[32] For this, both components were heat-treated at 98 °C for 5 h in a 500 mL flask. Once the reduction process was completed, black rGO was filtered through an alumina membrane (pore size = 200 nm, Whatman) with DI water and ethanol several times. Finally, rGO powder was obtained by vacuum drying at 70 °C for 12 h.

CNT-rGO$_{th}$ was prepared by a microwave-assisted polyol process.[50] 40 mg of CNTs (Hanwha Nanotech, Korea) was dispersed in 20 mL of ethylene glycol (Sigma Aldrich) by tip-sonication at 80 W for 5 h. Five milliliters of the GO solution (10 mg/mL) and 0.5 mL of sodium hydroxide solution (0.5 M, Sigma Aldrich) were then added into the CNT solution. After additional sonication for 1 h, the solution was processed in a household microwave oven (700 W) for 90 s. Next, the agglomerated powders were washed with acetone several times and dried at 70 °C under a vacuum for 12 h. The synthesis of CNT-rGO$_{th}$ was completed by a heat treatment at 800 °C under a vacuum (0.05 bar) for 1 h.

Characterizations. The chemical functional groups on the surfaces of the given samples were characterized by X-ray photoelectron spectroscopy (XPS, Thermo VG scientific, Sigma Probe). X-ray diffraction (XRD, Rigaku) was used to characterize the crystallinity of the graphitic array of each sample. The specific surface area, pore volume, and pore size distribution were obtained from N_2 adsorption−desorption measurements (Quantachrome, Quadrasorb SI). Field emission-scanning electron microscopy (FE-SEM, Sitrion) and field emission-transmission electron microscopy (FE-TEM, TECNAI) were employed to observe the morphologies of the samples.

All of the electrodes were fabricated by first preparing slurries consisting of the active materials, super-P (TIMCAL), and poly(vinylidene difluoride) (PVDF, Sigma Aldrich) dispersed in 1-methyl-2-pyrrolidine (NMP, Sigma Aldrich) in a mass ratio of 8:1:1. The slurries were cast onto Ni mesh, and the cast samples were dried in a vacuum oven at 70 °C for 12 h. The mass loading of the active materials was ~0.5 mg/cm^2 for all of the electrodes in this study. Cosolvents of ethylene carbonate (EC) and diethylene carbonate (DEC) (1:1 *v/v*) containing 1 M lithium hexafluorophosphate ($LiPF_6$) (PANAX E-TEC, Korea) were used as electrolyte. Porous membranes (Polypropylene, Celgard 2400) were used as separators, and 2032 coin-cells were assembled in an argon-filled glovebox. For actual electrochemical testing of all of the samples, the galvanostatic charge/discharge measurements were carried out in the voltage range of 0−2 V using a WBCS 3000 battery cycler (WonATech, Korea) and VMP3 (Bio Logic, France) at 25 °C. The specific capacitance (C_s, F/g), energy density (ED, Wh/kg), and power density (PD, W/kg) were attained from the galvanostatic results. The specific capacitance was obtained on the basis of the following equation:

$$C_s = I/[-\Delta V/\Delta t]m = I/[-\text{slope}]m$$

where *I*, *m*, and slope are the discharge current, the mass of the active material on one electrode, and the slope of the discharge curve after the *iR* drop, respectively. ED was calculated by multiplying the integration area of the galvanostatic discharge curve (voltage *versus* discharge time) with the current density (A/g). PD was calculated by dividing ED by discharge time. The exact equations for ED and PD are as follows:

$$\text{ED} = \int_0^t \frac{VI}{M} dt, \quad \text{PD} = \frac{1}{t} \int_0^t \frac{VI}{M} dt$$

where *V*, *M*, *I*, and *t* are the voltage, the mass of the active materials on both electrodes, the discharge current, and the discharge time, respectively.

Conflict of Interest: The authors declare no competing financial interest.

Acknowledgment. We acknowledge financial support by the National Research Foundation of Korea (NRF) grant funded by the Korea government (MEST) (NRF-2010-C1AAA001-0029031 and NRF-2012-M1A2A2026587).

Supporting Information Available: X-ray photoelectron spectroscopy (XPS) data, scanning transmission electron microscopy (STEM) images, high resolution scanning electron microscopy (SEM) images, the additional BET results, and Ragone plot. This material is available free of charge *via* the Internet at http://pubs.acs.org.

REFERENCES AND NOTES

1. Yang, Z. G.; Zhang, J. L.; Kintner-Meyer, M. C. W.; Lu, X. C.; Choi, D. W.; Lemmon, J. P.; Liu, J. Electrochemical Energy Storage for Green Grid. *Chem. Rev.* **2011**, *111*, 3577–3613.
2. Ibrahim, H.; Ilinca, A.; Perron, J. Energy Storage Systems—Characteristics and Comparisons. *Renewable Sustainable Energy Rev.* **2008**, *12*, 1221–1250.
3. Lee, J. H.; Shin, W. H.; Ryou, M. H.; Jin, J. K.; Kim, J.; Choi, J. W. Functionalized Graphene for High Performance Lithium Ion Capacitors. *ChemSusChem* **2012**, *5*, 2328–2333.
4. Kotz, R.; Carlen, M. Principles and Applications of Electrochemical Capacitors. *Electrochim. Acta* **2000**, *45*, 2483–2498.
5. Burke, A. Ultracapacitors: Why, How, and Where Is the Technology. *J. Power Sources* **2000**, *91*, 37–50.
6. Simon, P.; Gogotsi, Y. Materials for Electrochemical Capacitors. *Nat. Mater.* **2008**, *7*, 845–854.
7. Candelaria, S. L.; Shao, Y. Y.; Zhou, W.; Li, X. L.; Xiao, J.; Zhang, J. G.; Wang, Y.; Liu, J.; Li, J. H.; Cao, G. Z. Nanostructured Carbon for Energy Storage and Conversion. *Nano Energy* **2012**, *1*, 195–220.
8. Yu, G. H.; Xie, X.; Pan, L. J.; Bao, Z. N.; Cui, Y. Hybrid Nanostructured Materials for High-Performance Electrochemical Capacitors. *Nano Energy* **2013**, *2*, 213–234.
9. Armaroli, N.; Balzani, V. Towards an Electricity-Powered World. *Energy Environ. Sci.* **2011**, *4*, 3193–3222.
10. Choi, B. G.; Yang, M.; Hong, W. H.; Choi, J. W.; Huh, Y. S. 3d Macroporous Graphene Frameworks for Supercapacitors with High Energy and Power Densities. *ACS Nano* **2012**, *6*, 4020–4028.
11. Liu, C.; Li, F.; Ma, L. P.; Cheng, H. M. Advanced Materials for Energy Storage. *Adv. Mater.* **2010**, *22*, E28–E62.
12. El-Kady, M. F.; Strong, V.; Dubin, S.; Kaner, R. B. Laser Scribing of High-Performance and Flexible Graphene-Based Electrochemical Capacitors. *Science* **2012**, *335*, 1326–1330.
13. Jeong, H. M.; Lee, J. W.; Shin, W. H.; Choi, Y. J.; Shin, H. J.; Kang, J. K.; Choi, J. W. Nitrogen-Doped Graphene for High-Performance Ultracapacitors and the Importance of Nitrogen-Doped Sites at Basal Planes. *Nano Lett.* **2011**, *11*, 2472–2477.
14. Liu, C. G.; Yu, Z. N.; Neff, D.; Zhamu, A.; Jang, B. Z. Graphene-Based Supercapacitor with an Ultrahigh Energy Density. *Nano Lett.* **2010**, *10*, 4863–4868.

15. Stoller, M. D.; Park, S. J.; Zhu, Y. W.; An, J. H.; Ruoff, R. S. Graphene-Based Ultracapacitors. *Nano Lett.* **2008**, *8*, 3498–3502.
16. Yoon, Y.; Lee, K.; Baik, C.; Yoo, H.; Min, M.; Park, Y.; Lee, S. M.; Lee, H. Anti-Solvent Derived Non-Stacked Reduced Graphene Oxide for High Performance Supercapacitors. *Adv. Mater.* **2013**, 10.1002/adma.201301230.
17. Yun, Y. S.; Cho, S. Y.; Shim, J.; Kim, B. H.; Chang, S. J.; Baek, S. J.; Huh, Y. S.; Tak, Y.; Park, Y. W.; Park, S.; et al. Microporous Carbon Nanoplates from Regenerated Silk Proteins for Supercapacitors. *Adv. Mater.* **2013**, *25*, 1993–1998.
18. Zhu, Y. W.; Murali, S.; Stoller, M. D.; Ganesh, K. J.; Cai, W. W.; Ferreira, P. J.; Pirkle, A.; Wallace, R. M.; Cychosz, K. A.; Thommes, M.; et al. Carbon-Based Supercapacitors Produced by Activation of Graphene. *Science* **2011**, *332*, 1537–1541.
19. Wen, Z. H.; Wang, X. C.; Mao, S.; Bo, Z.; Kim, H.; Cui, S. M.; Lu, G. H.; Feng, X. L.; Chen, J. H. Crumpled Nitrogen-Doped Graphene Nanosheets with Ultrahigh Pore Volume for High-Performance Supercapacitor. *Adv. Mater.* **2012**, *24*, 5610–5616.
20. Hulicova-Jurcakova, D.; Seredych, M.; Lu, G. Q.; Bandosz, T. J. Combined Effect of Nitrogen- and Oxygen-Containing Functional Groups of Microporous Activated Carbon on Its Electrochemical Performance in Supercapacitors. *Adv. Funct. Mater.* **2009**, *19*, 438–447.
21. Wei, L.; Sevilla, M.; Fuertes, A. B.; Mokaya, R.; Yushin, G. Polypyrrole-Derived Activated Carbons for High-Performance Electrical Double-Layer Capacitors with Ionic Liquid Electrolyte. *Adv. Funct. Mater.* **2011**, *22*, 827–834.
22. Izadi-Najafabadi, A.; Yamada, T.; Futaba, D. N.; Yudasaka, M.; Takagi, H.; Hatori, H.; Iijima, S.; Hata, K. High-Power Supercapacitor Electrodes from Single-Walled Carbon Nanohorn/Nanotube Composite. *ACS Nano* **2011**, *5*, 811–819.
23. Frackowiak, E.; Beguin, F. Carbon Materials for the Electrochemical Storage of Energy in Capacitors. *Carbon* **2001**, *39*, 937–950.
24. Hu, L. B.; Choi, J. W.; Yang, Y.; Jeong, S.; La Mantia, F.; Cui, L. F.; Cui, Y. Highly Conductive Paper for Energy-Storage Devices. *Proc. Natl. Acad. Sci. U. S. A.* **2009**, *106*, 21490–21494.
25. Tai, Z. X.; Yan, X. B.; Lang, J. W.; Xue, Q. J. Enhancement of Capacitance Performance of Flexible Carbon Nanofiber Paper by Adding Graphene Nanosheets. *J. Power Sources* **2012**, *199*, 373–378.
26. Masarapu, C.; Zeng, H. F.; Hung, K. H.; Wei, B. Q. Effect of Temperature on the Capacitance of Carbon Nanotube Supercapacitors. *ACS Nano* **2009**, *3*, 2199–2206.
27. Si, P.; Ding, S. J.; Lou, X. W.; Kim, D. H. An Electrochemically Formed Three-Dimensional Structure of Polypyrrole/Graphene Nanoplatelets for High-Performance Supercapacitors. *RSC Adv.* **2011**, *1*, 1271–1278.
28. Yang, X.; Cheng, C.; Wang, Y.; Qiu, L.; Li, D. Liquid-Mediated Dense Intregration of Graphene Materials for Compact Capacitive Energy Storage. *Science* **2013**, *341*, 534–537.
29. Xia, J. L.; Chen, F.; Li, J. H.; Tao, N. J. Measurement of the Quantum Capacitance of Graphene. *Nat. Nanotechnol.* **2009**, *4*, 505–509.
30. Lv, W.; Tang, D. M.; He, Y. B.; You, C. H.; Shi, Z. Q.; Chen, X. C.; Chen, C. M.; Hou, P. X.; Liu, C.; Yang, Q. H. Low-Temperature Exfoliated Graphenes: Vacuum-Promoted Exfoliation and Electrochemical Energy Storage. *ACS Nano* **2009**, *3*, 3730–3736.
31. Zhu, Y. W.; Stoller, M. D.; Cai, W. W.; Velamakanni, A.; Piner, R. D.; Chen, D.; Ruoff, R. S. Exfoliation of Graphite Oxide in Propylene Carbonate and Thermal Reduction of the Resulting Graphene Oxide Platelets. *ACS Nano* **2010**, *4*, 1227–1233.
32. Stankovich, S.; Dikin, D. A.; Piner, R. D.; Kohlhaas, K. A.; Kleinhammes, A.; Jia, Y.; Wu, Y.; Nguyen, S. T.; Ruoff, R. S. Synthesis of Graphene-Based Nanosheets Via Chemical Reduction of Exfoliated Graphite Oxide. *Carbon* **2007**, *45*, 1558–1565.
33. Dreyer, D. R.; Park, S.; Bielawski, C. W.; Ruoff, R. S. The Chemistry of Graphene Oxide. *Chem. Soc. Rev.* **2010**, *39*, 228–240.
34. Acik, M.; Mattevi, C.; Gong, C.; Lee, G.; Cho, K.; Chhowalla, M.; Chabal, Y. J. The Role of Intercalated Water in Multilayered Graphene Oxide. *ACS Nano* **2010**, *4*, 5861–5868.
35. Marcano, D. C.; Kosynkin, D. V.; Berlin, J. M.; Sinitskii, A.; Sun, Z. Z.; Slesarev, A.; Alemany, L. B.; Lu, W.; Tour, J. M. Improved Synthesis of Graphene Oxide. *ACS Nano* **2010**, *4*, 4806–4814.
36. Zhu, Y. W.; Murali, S.; Cai, W. W.; Li, X. S.; Suk, J. W.; Potts, J. R.; Ruoff, R. S. Graphene and Graphene Oxide: Synthesis, Properties, and Applications. *Adv. Mater.* **2010**, *22*, 3906–3924.
37. Hummers, W. S.; Offeman, R. E. Preparation of Graphitic Oxide. *J. Am. Chem. Soc.* **1958**, *80*, 1339–1339.
38. Hulicova, D.; Yamashita, J.; Soneda, Y.; Hatori, H.; Kodama, M. Supercapacitors Prepared from Melamine-Based Carbon. *Chem. Mater.* **2005**, *17*, 1241–1247.
39. Jeong, H. M.; Lee, S. Y.; Shin, W. H.; Kwon, J. H.; Shakoor, A.; Hwang, T. H.; Kim, S. Y.; Kong, B. S.; Seo, J. S.; Lee, Y. M.; et al. Silicon@Porous Nitrogen-Doped Carbon Spheres through a Bottom-up Approach Are Highly Robust Lithium-Ion Battery Anodes. *RSC Adv.* **2012**, *2*, 4311–4317.
40. Friedel, B.; Greulich-Weber, S. Preparation of Monodisperse, Submicrometer Carbon Spheres by Pyrolysis of Melamine-Formaldehyde Resin. *Small* **2006**, *2*, 859–863.
41. Raymundo-Pinero, E.; Cazorla-Amoros, D.; Linares-Solano, A.; Find, J.; Wild, U.; Schlogl, R. Structural Characterization of N-Containing Activated Carbon Fibers Prepared from a Low Softening Point Petroleum Pitch and a Melamine Resin. *Carbon* **2002**, *40*, 597–608.
42. Drage, T. C.; Arenillas, A.; Smith, K. M.; Pevida, C.; Piippo, S.; Snape, C. E. Preparation of Carbon Dioxide Adsorbents from the Chemical Activation of Urea-Formaldehyde and Melamine-Formaldehyde Resins. *Fuel* **2007**, *86*, 22–31.
43. McAllister, M. J.; Li, J. L.; Adamson, D. H.; Schniepp, H. C.; Abdala, A. A.; Liu, J.; Herrera-Alonso, M.; Milius, D. L.; Car, R.; Prud'homme, R. K.; et al. Single Sheet Functionalized Graphene by Oxidation and Thermal Expansion of Graphite. *Chem. Mater.* **2007**, *19*, 4396–4404.
44. Moon, I. K.; Lee, J.; Ruoff, R. S.; Lee, H. Reduced Graphene Oxide by Chemical Graphitization. *Nat. Commun.* **2010**, 10.1038/ncomms1067.
45. Brunauer, S.; Emmett, P. H.; Teller, E. Adsorption of Gases in Multimolecular Layers. *J. Am. Chem. Soc.* **1938**, *60*, 309–319.
46. Banks, C. E.; Davies, T. J.; Wildgoose, G. G.; Compton, R. G. Electrocatalysis at Graphite and Carbon Nanotube Modified Electrodes: Edge-Plane Sites and Tube Ends Are the Reactive Sites. *Chem. Commun.* **2005**, 829–841.
47. Yang, S. Y.; Chang, K. H.; Tien, H. W.; Lee, Y. F.; Li, S. M.; Wang, Y. S.; Wang, J. Y.; Ma, C. C. M.; Hu, C. C. Design and Tailoring of a Hierarchical Graphene-Carbon Nanotube Architecture for Supercapacitors. *J. Mater. Chem.* **2011**, *21*, 2374–2380.
48. Pandolfo, A. G.; Hollenkamp, A. F. Carbon Properties and Their Role in Supercapacitors. *J. Power Sources* **2006**, *157*, 11–27.
49. Kosynkin, D. V.; Higginbotham, A. L.; Sinitskii, A.; Lomeda, J. R.; Dimiev, A.; Price, B. K.; Tour, J. M. Longitudinal Unzipping of Carbon Nanotubes to Form Graphene Nanoribbons. *Nature* **2009**, *458*, 872–876.
50. Shin, W. H.; Jeong, H. M.; Kim, B. G.; Kang, J. K.; Choi, J. W. Nitrogen-Doped Multiwall Carbon Nanotubes for Lithium Storage with Extremely High Capacity. *Nano Lett.* **2012**, *12*, 2283–2288.